PAPER • **OPEN ACCESS**

Quantum logical controlled-NOT gate in a lithium niobate-on-insulator photonic quantum walk

To cite this article: Robert J Chapman *et al* 2024 *Quantum Sci. Technol.* **9** 015016

IOP Publishing Quantum Sci. Technol. 9 (2024) 015016 https://doi.org/10.1088/2058-9565/ad0a48

Quantum Science and Technology

OPEN ACCESS

RECEIVED
5 July 2023

REVISED
12 October 2023

ACCEPTED FOR PUBLICATION
7 November 2023

PUBLISHED
17 November 2023

PAPER

Quantum logical controlled-NOT gate in a lithium niobate-on-insulator photonic quantum walk

Robert J Chapman[1,*], **Samuel Häusler**[2], **Giovanni Finco**[1], **Fabian Kaufmann**[1] and **Rachel Grange**[1]

[1] Optical Nanomaterial Group, Institute for Quantum Electronics, Department of Physics, ETH Zurich, CH-8093 Zurich, Switzerland
[2] Institute for Sensors and Electronics, University of Applied Sciences and Arts Northwestern Switzerland, CH-5210 Windisch, Switzerland
[*] Author to whom any correspondence should be addressed.

E-mail: rchapman@phys.ethz.ch

Keywords: quantum photonics, integrated photonics, quantum information, quantum logic gates, lithium niobate on insulator

Supplementary material for this article is available online

Abstract

The two-qubit controlled-NOT gate is one of the central entangling operations in quantum information technology. The controlled-NOT gate for single photon qubits is normally realized as a network of five individual beamsplitters on six optical modes. Quantum walks (QWs) are an alternative photonic architecture involving arrays of coupled waveguides, which have been successful for investigating condensed matter physics, however, have not yet been applied to quantum logical operations. Here, we engineer the tight-binding Hamiltonian of an array of lithium niobate-on-insulator waveguides to experimentally demonstrate the two-qubit controlled-NOT gate in a QW. We measure the two-qubit transfer matrix with 0.938 ± 0.003 fidelity, and we use the gate to generate entangled qubits with 0.945 ± 0.002 fidelity by preparing the control photon in a superposition state. Our results highlight a new application for QWs that use a compact multi-mode interaction region to realize large multi-component quantum circuits.

Photonic quantum information technologies use controlled superposition and entangled single photon qubits for applications in quantum computing [1, 2], simulation [3], communication [4] and sensing [5]. At the core of any quantum information processor is the ability to entangle qubits via logical operation such as the controlled-NOT (CNOT) gate, which is fundamental to many leading quantum computing algorithms. These operations are typically the most challenging to perform, as the qubits must interact with each other but be otherwise fully isolated to preserve coherence [6]. In linear optical quantum computing, photonic qubits are entangled by quantum interference at beamsplitters and single photon detection, either in post-selection or by heralding ancillary photons [7]. The typical linear optical CNOT gate is realized in a six-mode interferometer comprising five beamsplitters [8] and has been demonstrated in free-space optics with polarization encoding [9], and in integrated photonics with path encoding [10]. Four modes are for the two qubits and the extra modes provide loss channels that are necessary to balance the probabilistic logical operation. The need for high-fidelity entangling gates puts stringent requirements on the accuracy of the beamsplitter reflectivities, stability of the interferometer and indistinguishability of the single photons in all degrees of freedom. Photonic integrated circuits benefit from the precision and inherent phase stability of monolithic nanofabricated devices, and comprise optical waveguides for routing light on-chip, directional couplers (DCs) or multi-mode interferometers that act as two-mode beamsplitters, and thermo- or electro-optic phase control for reconfigurability. It is known that a nest of two-mode interferometers can be configured for any linear optical unitary, including the CNOT gate, however, this architecture is dominated by routing of light between separate beamsplitters, which does not contribute to the logical operation [11, 12].

Quantum walks (QWs) are an alternative photonics architecture, realized as arrays of coupled waveguides where light interferes along the entire propagation length instead of at individual beamsplitters.

The optical evolution in the QW is described by a tight-binding Hamiltonian that can be engineered for many applications and for studying fundamental physics. This includes the experimental demonstration of topologically bound states [13–18], Anderson localization [19–23], quantum transport [24, 25] and for preparing large single photon superposition states [26]. When pairs of indistinguishable photons propagate in a QW, they undergo bosonic bunching similar to the Hong–Ou–Mandel (HOM) effect, which has been observed in free-space optics [27], multi-mode fiber-optics [28] and integrated photonics [29]. It has been recently proposed that multi-mode quantum interference in a specifically parameterized six-waveguide array can implement the CNOT gate on path-encoded photonic qubits [30]. In this realization of the CNOT gate, the photons interfere continuously along the length of the array, removing the need for on-chip routing. However, such a device is challenging to produce because of the precise control required on the tight-binding Hamiltonian for each propagation and hopping term. While sophisticated QWs have been demonstrated in several photonics technologies, controlled two-qubit gates are yet to be realized.

Here, we experimentally demonstrate the two-qubit CNOT gate realized in a continuous time QW. We fabricated the six-waveguide 'QW-CNOT' array in lithium niobate-on-insulator (LNOI) and fully control the on-site energies and nearest-neighbor hopping of the tight-binding Hamiltonian in the design of the individual waveguide widths and separations respectively. We measure the two-qubit CNOT transfer matrix with a fidelity of 0.938 ± 0.003 using photons generated by spontaneous parametric down-conversion (SPDC). The reduced fidelity is due to the limited indistinguishability of the SPDC source, bandwidth of the QW controlled-NOT (QW-CNOT) chip and fiber dispersion. We also prepare the control qubit in the $\frac{1}{\sqrt{2}}(|0\rangle + e^{i\phi}|1\rangle)$ superposition state using an on-chip DC and use the QW-CNOT gate to generate the state $\frac{1}{\sqrt{2}}(|00\rangle + e^{i\phi}|11\rangle)$ with fidelity 0.945 ± 0.002, measured in the computational basis. The addition of on-chip phase control would enable generation of maximally entangled Bell states, which are an important resource for quantum computing and quantum communication. Our results open a pathway towards implementing large multi-mode photonic circuits in a single step using QWs.

1. Results

1.1. Quantum controlled-NOT gate in a photonic QW

The QW-CNOT gate operates on path encoded control $|c\rangle$ and target $|t\rangle$ qubits, that are superposition states of photon occupation across pairs of neighboring waveguides. The evolution of the QW is described by the tight-binding Hamiltonian

$$h = \sum_{i=1}^{N} \beta_i \hat{a}_i^\dagger \hat{a}_i + \sum_{i=1}^{N-1} \kappa_i \left(\hat{a}_i^\dagger \hat{a}_{i+1} + \hat{a}_{i+1}^\dagger \hat{a}_i \right), \tag{1}$$

which is the sum of the propagation coefficients of each waveguide $\beta_i = 2\pi\, n_{\mathrm{eff},i}/\lambda$ and the coupling rates between neighboring waveguides κ_i. The unitary operation is described by Schrödinger's equation $U = \exp(-iht)$ for an evolution time t. Lahini *et al* determined the specific six waveguide tight-binding Hamiltonian with an equivalent unitary to the traditional linear optical CNOT gate [30], which is usually realized as a network of five beamsplitters [8] (shown in supplementary section 1). The QW-CNOT requires the Hamiltonian-time product

$$ht = \pi \begin{pmatrix} 0 & -1.27 & 0 & 0 & 0 & 0 \\ -1.27 & -0.73 & 0 & 0 & 0 & 0 \\ 0 & 0 & 0.67 & -0.51 & 0 & 0 \\ 0 & 0 & -0.51 & 0.01 & -1.69 & 0 \\ 0 & 0 & 0 & -1.69 & -1.01 & -0.52 \\ 0 & 0 & 0 & 0 & -0.52 & -1.67 \end{pmatrix}, \tag{2}$$

where diagonal terms correspond to the propagation coefficients β_i and the off-diagonal terms correspond to the nearest-neighbor hopping rates κ_i. The two-photon evolution for each input state is shown in figure 1 for the reduced logical subspace. Four waveguides are required to encode the two qubits and two additional auxiliary modes that allow the photons to propagate in a larger Hilbert space that is subsequently reduced by post-selection. Figures 1(a) and (b) show the control qubit in the $|0\rangle$ state where it is decoupled from the rest of the array and does not interfere with the target qubit. Coupling to the auxiliary modes and to other non-logical modes are not shown in this evolution, but can be seen in the complete Hilbert space (shown in supplementary section 2). Figures 1(c) and (d) show the control qubit in the $|1\rangle$ state, where it quantum interferes with the target qubit. Quantum interference between the two photons leads to a bit-flip operation

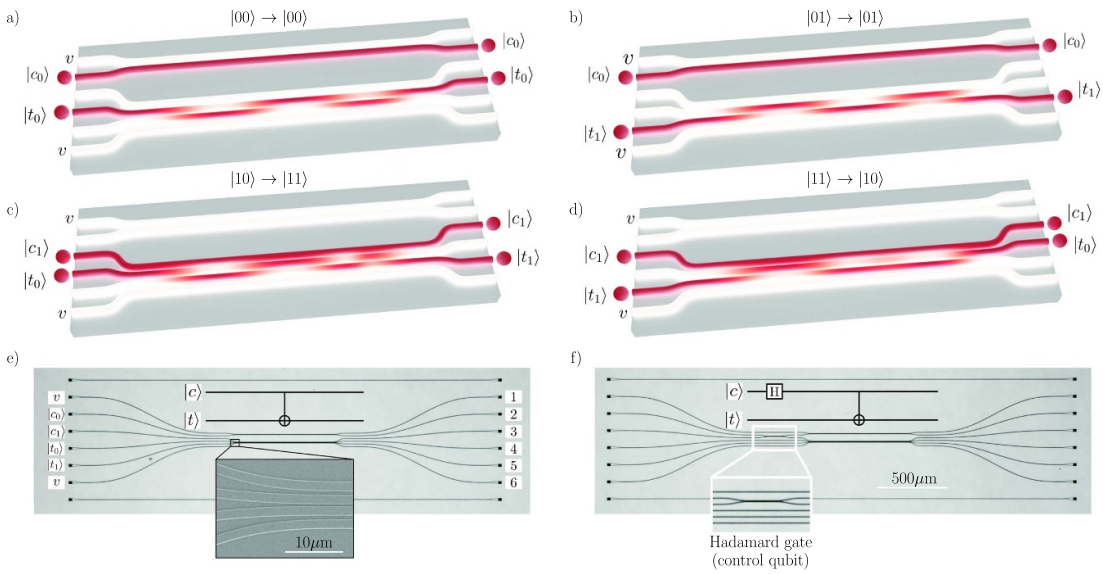

Figure 1. Evolution of the QW-CNOT device. Two-qubit evolution in the QW-CNOT waveguide array shown in the two-qubit logical subspace for input states $|ct\rangle$: (a) $|00\rangle$, (b) $|01\rangle$, (c) $|10\rangle$, and (d) $|11\rangle$. Labels $|c\rangle$ and $|t\rangle$ indicate the control and target qubits, and the input waveguides labeled v are auxiliary modes. When the control qubit is in the $|1\rangle$ state the photon interferes with the target qubit and causes a bit-flip operation. This operation is only possible when post-selecting the logical subspace. (e) A microscope image of the QW-CNOT realized in the LNOI photonics platform. The labels on the left show the qubit encoding and on the right the waveguide number. The inset shows a scanning electron micrograph of the start of the coupling region. (f) A microscope image of the QW-CNOT array with an additional DC that implements a Hadamard gate, labeled H, preparing the control qubit in a superposition state.

on the target qubit. The visualization here does not consider the amplitude of the state within the two-qubit subspace where each of the logical transformations has a 1/9 success probability (shown in supplementary section 2).

1.2. QW-CNOT design and fabrication

We use the LNOI photonics platform to implement a QW-CNOT gate with waveguides designed for 1550 nm wavelength and transverse electric polarization. LNOI has a broad transparency range, low loss, and high electro-optic and $\chi^{(2)}$ nonlinear coefficients, making it a leading technology for photonic quantum information processors [31]. LNOI has become a major focus in photonics research, with demonstrations of record high-speed and low-voltage modulation [32], ultra-efficient nonlinear frequency conversion [33], all-optical switching [34] and entangled photon pair generation [35]. We etch the waveguide array in a 300 nm LN film with a 4.7 μm SiO_2 bottom oxide on a silicon handle wafer [36]. The etched waveguide height is 230 nm and we use the width and separation to control the propagation coefficients β_i and coupling rates κ_i in the tight-binding Hamiltonian. We exchange time-evolution for equivalent length-evolution for designing the array and target an array length $L = 700\,\mu$m such that the Hamiltonian-length product hL matches equation (2). We chose the on-site terms to be relative about the first waveguide which we set to 1.5 μm width and which defines the value of β_1. We simulate the mode for various waveguide widths using a finite-element solver and plot the corresponding value of $\Delta\beta_i L/\pi = (\beta_i - \beta_1)L/\pi$ in figure 2(a). The inset in figure 2(a) shows the typical waveguide cross section and solution of the fundamental transverse electric mode.

Using the determined waveguide widths, we simulate the even and odd supermodes of neighboring waveguides to calculate the coupling rate as $\kappa = \pi(n_{\text{even}} - n_{\text{odd}})/\lambda$, as shown in figure 2(b). The points indicate the necessary parameters for the Hamiltonian. Note that there is no hopping between waveguides 2 and 3 in the Hamiltonian as $\kappa_2 = 0$. The waveguide numbering is shown in figure 1(e), and we position waveguides 2 and 3 with a $\sim$50 μm gap to effectively decouple the modes. Figures 1(e) shows a microscope image of the QW-CNOT and figure 1(f) shows another device on the same chip with an additional DC that prepares the control qubit in a superposition state. The different waveguide separations can be seen in the scanning electron micrograph and reflects the different coupling coefficients of the Hamiltonian. The total footprint of our QW-CNOT gate is 700 μm $\times$ 65 μm. The length is defined by the number of hops to neighboring waveguides that is dictated by the Hamiltonian-length product. It would be possible to shorten the array by increasing the coupling strength, however, at a cost of greater sensitivity of the β and κ terms.

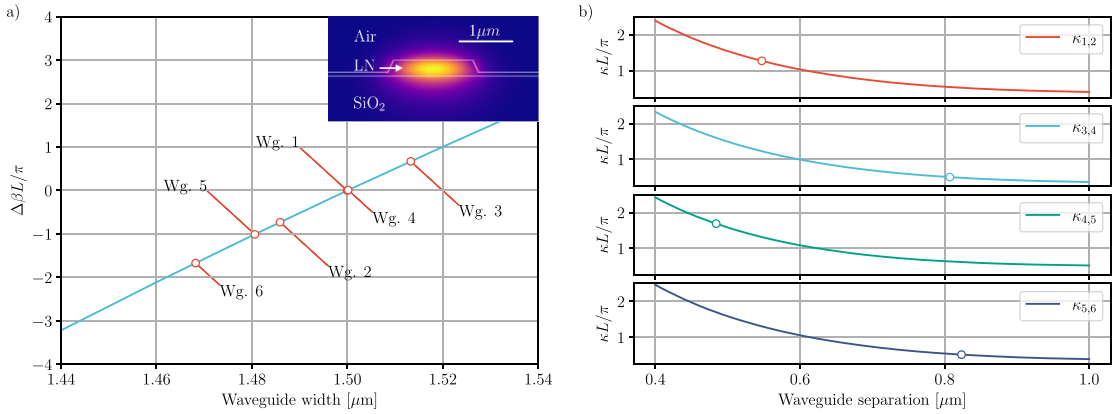

Figure 2. Design of the QW-CNOT array in LNOI photonics. (a) The dependence of the propagation coefficient β on the waveguide width (top edge) with a fixed etch depth of 230 nm and remaining film of 70 nm. The required waveguide widths are indicated on the curve. The inset shows the fundamental transverse electric mode of the LNOI waveguide. (b) The dependence of the coupling coefficient κ on the waveguide separation (edge to edge) for each of the coupled waveguides. Waveguides 2 and 3 are not coupled as $\kappa_2 = 0$ in the Hamiltonian.

The total coupling region involves ∼2.3 hopping lengths between the first two waveguides. This is marginally longer than the total ∼1.6 hopping length of the traditional CNOT gate based on DCs. However, this does not take into account bends between individual DCs which for some photonics platforms can have bend radii an order of magnitude larger than the hopping length [10].

Our fabrication process achieves a typical width and separation tolerance of 10 nm. Variations in waveguide width or separation are observed collectively for all waveguides, and not as randomized errors [36]. We performed a Monte Carlo simulation of the impact of width and separation errors and estimate a fidelity of the CNOT operation of 0.996 ± 0.003 with a uniformly distributed error of 10 nm (see supplementary section 2 for details on the impact of fabrication errors on the fidelity). Interestingly, the propagation coefficients in figure 2(a) have width variations less than 10 nm, yet a collective variation has only a small impact on the fidelity.

We couple light to the chip using grating couplers with ∼6 dB loss per coupler. Grating couplers offer several advantages over end-fire coupling, such as eliminating the need for dicing and polishing waveguide facets, larger mode field diameters, and polarization sensitivity, ensuring the excitation of only the waveguide transverse electric mode. Higher efficiency grating couplers in LNOI have been reported [37–39] with losses as low as ∼1 dB per grating [40]. Recently, grating couplers in silicon nitride were demonstrated with ∼0.5 dB loss, which could be also feasible with LNOI [41].

1.3. Classical characterization

To classically characterize the QW-CNOT gate, we inject a 1550 nm wavelength continuous-wave laser into each input of the chip and record the intensity at all the outputs with a near-infrared camera. Figure 3 shows the propagation simulation based on the Hamiltonian in equation (2), as well as measured output intensity distributions for each of the six inputs in the waveguide array. The propagation here differs from the two-photon evolution shown in figure 1 as only a single mode is excited. We calculate the fidelity between the experimental transfer matrix Γ and the theoretical transfer matrix Γ' as

$$F(\Gamma,\Gamma') = \sum_{i,j}\sqrt{\frac{\Gamma_{i,j}\Gamma'_{i,j}}{\left(\sum_{i,j}\Gamma_{i,j}\right)\left(\sum_{i,j}\Gamma'_{i,j}\right)}}. \tag{3}$$

The fidelity between the classically characterized transfer matrix and the theoretical model is 0.982 ± 0.007 where the error is calculated from the variation in fidelity for each waveguide input. From this characterization, we can build a simulation of the device by finding the Hamiltonian that gives the closest match to the measured output. This simulation will be a tool for predicting the two-photon dynamics of the QW-CNOT chip.

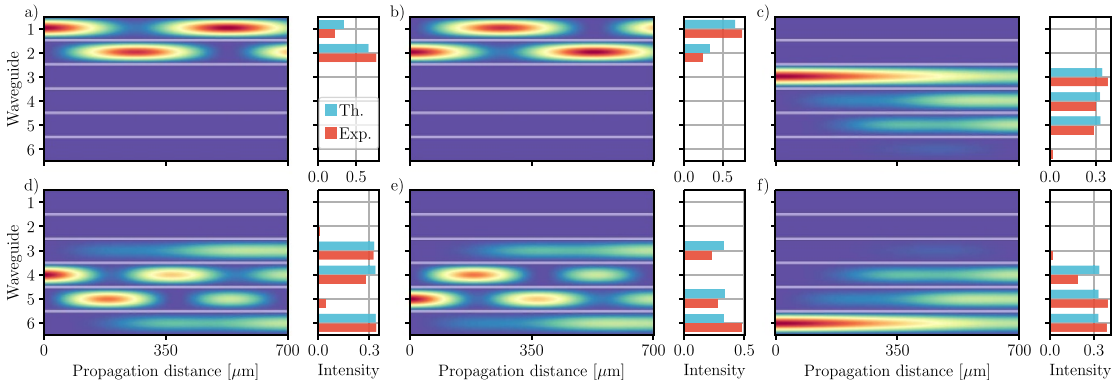

Figure 3. Classical characterization. The theoretical evolution intensity in the QW-CNOT chip for each of the six waveguide inputs. The output intensity for each evolution is shown for the theoretical model (blue) and the experimental result (red). The theoretical evolution is calculated from the Hamiltonian in equation (1) with the values of β and κ shown in figure 2.

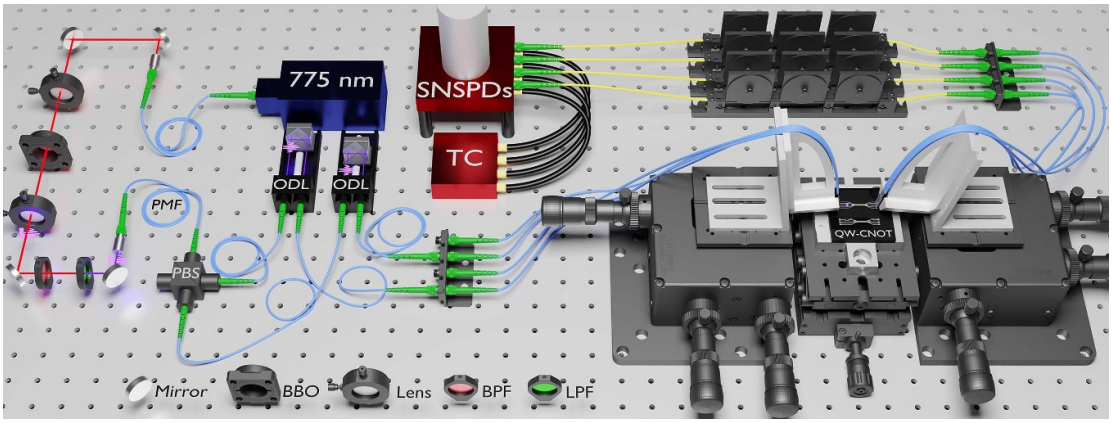

Figure 4. Experimental setup. Orthogonally polarized photon-pairs are generated by type-2 spontaneous parametric down-conversion in a 2 mm thick beta barium borate (BBO) crystal and the pump is filtered with a longpass filter (LPF) and the photons with a 12 nm bandpass filter (BPF). The photons are coupled to polarization maintaining fiber (PMF) and separated with a polarizing beamsplitter (PBS) where one fiber pigtail is rotated such that both photons have the same output polarization. The photons are injected into optical delay lines (ODLs) to compensate for fiber length mismatch and fiber birefringence and are coupled to the QW-CNOT chip with a fiber array positioned above on-chip grating couplers. After the QW, the photons are collected in fiber and measured with superconducting nanowire single photon detectors (SNSPDs) and the arrival times are recorded with a time correlator (TC). Polarization controllers are used to maximize the efficiency of the SNSPDs.

1.4. SPDC source and experimental setup

In order to measure the two-qubit operation of the QW-CNOT gate, we require a source of indistinguishable photons at 1550 nm wavelength. To achieve this, we employ a collinear type-2 SPDC process using a beta-barium borate crystal. A diagram of the complete experimental setup is depicted in figure 4. We use a 775 nm continuous-wave laser to pump the nonlinear crystal, generating photon pairs which are filtered with a 12 nm bandpass filter to ensure both photons have the same bandwidth. Because we use a type-2 SPDC process, one photon is horizontally polarized and the other vertically polarized. We couple both photons into a polarization maintaining fiber and separate them with a fiber-pigtailed polarizing beamsplitter. One of the output fibers is pigtailed with the slow axis vertical and the other fiber with the slow axis horizontal, so that both photons exit the beamsplitter with the same polarization in each fiber. Motor-controlled optical delay lines compensate for mismatch in fiber lengths and birefringence before the photons are coupled to the chip. Photons are coupled to and from the chip with fiber arrays positioned above the grating couplers with precision translation stages. Finally, coincidence measurements are performed with superconducting nanowire single photon detectors and a time correlator to record arrival times. We verify the indistinguishability of the generated photons through the characteristic HOM dip, measured by interfering the photons in a fused-silica 50:50 beamsplitter with 94.6% visibility (further details in supplementary section 3). Narrower bandpass filters can improve the source visibility by reducing fiber dispersion at the cost of lowering the photon count rate.

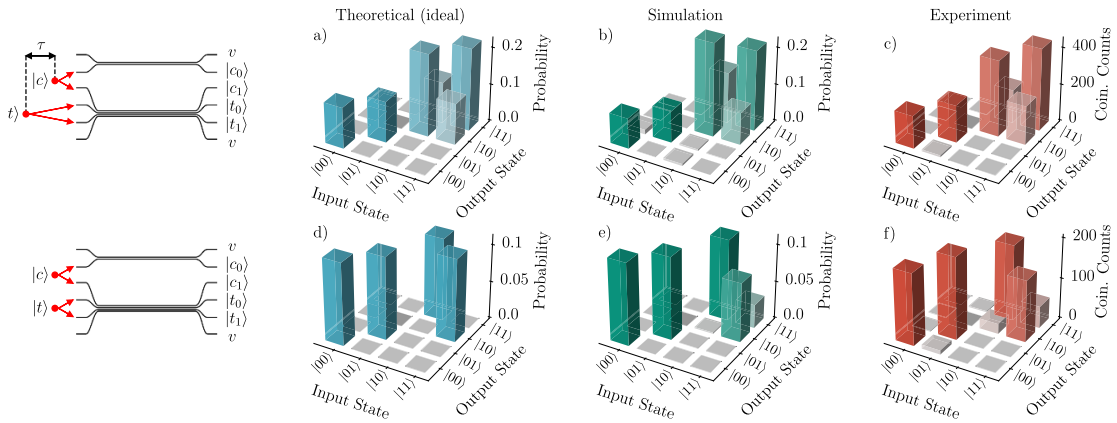

Figure 5. Two-qubit transfer matrix. (a)–(c) The theoretical (ideal), simulated and experimental two-qubit transfer matrix when the photons arrive with a time separation τ. In this regime, the photons do not quantum interfere. (d)–(f) The theoretical (ideal), simulated and experimental two-qubit transfer matrix with indistinguishable photons that arrive with zero time delay.

1.5. QW-CNOT array two-qubit transfer matrix

The operation of the two-qubit QW-CNOT chip is based on quantum interference between the control and target qubits. The control $|0\rangle$ state does not interfere with the target qubit and thus the arrival time of the two photons has no impact on the transfer matrix. However, for the control $|1\rangle$ state, the photon arrival times are critical to allow for interference. We use the motorized optical delay lines to match the arrival times of the control and target qubits. For the input state $|10\rangle$, we observe HOM interference between waveguides 3 and 4, which results in suppression of the output state $|10\rangle$ and therefore only the logical output $|11\rangle$ is measured. Likewise for input state $|11\rangle$, HOM interference is observed between waveguides 3 and 5, meaning only the logical output $|10\rangle$ is measured. This interference gives rise to the logical CNOT operation in our chip. The raw HOM interference plots are shown in supplementary section 4. We measure the two-qubit transfer matrix of the QW-CNOT chip with and without a delay between the photons and plot the results in figure 5. When the photons arrive at the chip with a time delay (τ), there is no quantum interference and we observe classical propagation dynamics. In figures 5(a)–(c), we show the ideal theoretical, simulation and experimental results respectively. Because there is no quantum interference, the simulation is simply the product of the classical probability distributions shown in figure 3. We calculate the fidelity using equation (3) between the theoretical model and the experiment as 0.994 ± 0.001 and between the simulation and the experiment as 0.991 ± 0.001, where errors are calculated using Poissonian statistics.

We scan the optical delay lines and measure HOM interference between the control and target photons in the QW-CNOT waveguide array. When the delay is $\tau = 0$, the photons arrive simultaneously and the CNOT operation is implemented by quantum interference. The theoretical, simulated and experimentally measured transfer matrices are shown in figures 5(d)–(f) respectively. The fidelity between the theoretical model and the experiment is 0.938 ± 0.003 and between the simulation and the experiment is 0.991 ± 0.001. The reduced fidelity of the two-photon interference is attributed to the relatively broad bandwidth of the SPDC photons (12 nm), meaning optical dispersion in fibers and waveguide, and the sensitivity of the Hamiltonian to wavelength, decrease the visibility of the two-qubit interference.

1.6. Entangled state generation

The CNOT gate is a fundamental element for quantum computation and can be used to prepare maximally entangled Bell states when the control qubit is in the superposition state $|c\rangle = \frac{1}{\sqrt{2}}(|0\rangle \pm |1\rangle)$ and the target qubit in either the $|0\rangle$ or $|1\rangle$ state. We fabricated a QW-CNOT gate with the addition of a DC that prepares the control qubit in the superposition state $|c\rangle = \frac{1}{\sqrt{2}}(|0\rangle + e^{i\phi}|1\rangle)$ and the target qubit is kept in the $|0\rangle$ state. In this work, we do not set the phase ϕ of the control qubit before the QW-CNOT gate, which would be necessary to prepare a maximally entangled Bell state. However, electro-optic and thermo-optic phase shifters are well established technologies in integrated photonics. Switching networks have been realized in LNOI photonics using both electro-optic [42] and thermo-optic phase shifters [43]. In particular for LNOI photonics, electro-optics has the advantage of reduced cross talk between neighboring waveguides, and can switch at high speeds. When the two photons arrive with a time delay τ, the input state becomes an incoherent mixture $\frac{1}{2}(|00\rangle\langle 00| + |10\rangle\langle 10|)$ and no quantum interference is observed. The expected output of the QW-CNOT in this case is $\frac{1}{4}(|00\rangle\langle 00| + 2|10\rangle\langle 10| + |11\rangle\langle 11|)$. On the other hand, when the photons arrive simultaneously, i.e $\tau = 0$, the input state is a coherent superposition $\frac{1}{\sqrt{2}}(|00\rangle + e^{i\phi}|10\rangle)$ and the

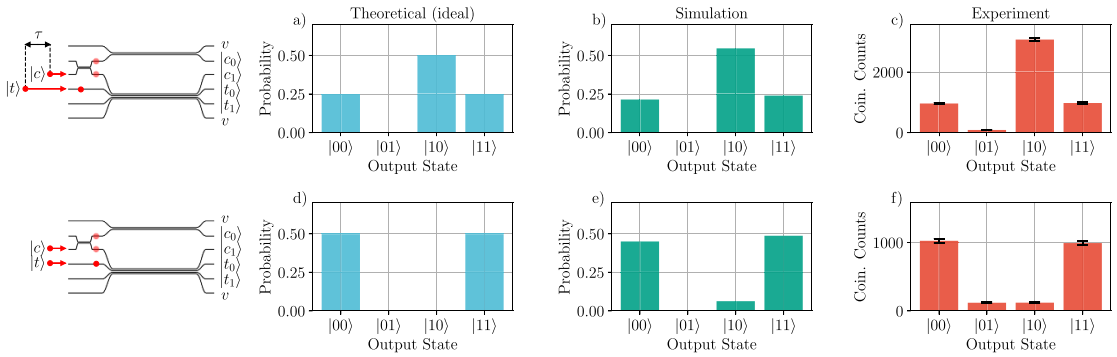

Figure 6. Entangled state preparation. A directional coupler is included before the QW-CNOT array to prepare the control qubit in a superposition state $(|0\rangle + e^{i\phi}|1\rangle)/\sqrt{2}$. (a)–(c) The theoretical (ideal), simulated and experimental two-qubit output when the photons arrive with a time difference τ. This means the two qubits are distinguishable and no entanglement is generated. (d)–(f) The theoretical (ideal), simulated and experimental two-qubit output when the photons arrive together and undergo HOM interference. In this case, the entangled state $(|00\rangle + e^{i\phi}|11\rangle)/\sqrt{2}$ is generated. The error bars in (c) and (f) are calculated from Poissonian statistics.

Table 1. Summary of the measured fidelities of the QW-CNOT device. The classical characterization is only compared to the theoretical value and is the basis for the QW-CNOT gate fidelity.

Experiment	Fidelity to theoretical value	Fidelity to simulation
Classical transfer matrix (mixed)	0.982 ± 0.007	N/A
CNOT transfer matrix (mixed)	0.994 ± 0.001	0.991 ± 0.001
CNOT transfer matrix (pure)	0.938 ± 0.003	0.985 ± 0.002
Bell state preparation (mixed)	0.985 ± 0.001	0.987 ± 0.001
Bell state preparation (pure)	0.945 ± 0.002	0.973 ± 0.001

expected output is the entangled state $\frac{1}{\sqrt{2}}(|00\rangle + e^{i\phi}|11\rangle)$. On the same device, we fabricated a network of DCs with the same parameters in order to characterize the splitting ratio. We measure a DC reflectivity of 0.551 ± 0.002 and we consider this imbalance in our simulated output of the QW-CNOT. The entangled state preparation results are presented in figure 6. Based on the two-photon transfer matrix measured previously, we construct a model of the two-qubit entangled state preparation. The theoretical, simulated and measured output for the incoherent input state, measured in the computational basis, are shown in figures 6(a)–(c) respectively. We measured a greater probability of $|10\rangle$ output than expected from our simulations, even when taking into account the imbalance of the DC. We attribute this difference to imbalanced output chip to fiber coupling efficiencies, and to differences between the two QW-CNOT arrays fabricated on the chip. It is known that current LNOI wafer material suffers from inhomogeneities, for example in the film thickness, which can lead to variations in device performance even on the same chip [44]. We calculate the fidelity between the theoretical state and the experiment as 0.985 ± 0.001 and between the simulated state and the experiment as 0.987 ± 0.001. The theoretical, simulated and measured output for the coherent superposition input state are shown in figures 6(d)–(f) respectively. The fidelity between the theoretical output and the experiment is 0.945 ± 0.002 and between the simulation and experiment is 0.973 ± 0.001. Although these results are from a different QW-CNOT device, the experiment and simulation show good agreement. The fidelity here assumes $\phi = 0$, which can be achieved with an on-chip phase shifter for the input control qubit. The two-qubit entangled state could be verified by performing two-qubit state tomography or violating the Clauser, Horn, Shimony and Holt (CHSH) inequality [45]. Nevertheless, this experiment shows the QW-CNOT device is capable of performing photonic entangling gates in a single interaction step, which could provide a significant improvement over the traditional multi-step circuit approach.

2. Discussion

We have successfully implemented the controlled-NOT gate in a continuous-time QW on the LNOI photonics platform, and have summarized the performance in table 1. Using indistinguishable photons from a SPDC source, we have measured the transfer matrix of the two-qubit CNOT gate, and prepared the control qubit in a superposition leading to the generation of entangled states. Tunable waveguide arrays are being actively researched, using thermo- and electro-optics to reconfigure the dynamics of QWs in silica and proton-exchange LN waveguides [46, 47]. Adding electro-optic tunability to the QW-CNOT device could

compensate for chip variations when scaling up to multiple gates. In particular, electro-optics could be used to locally change the β and κ terms of the Hamiltonian with minimal cross-talk because of the shielding effect of each electrode, similar to the technique demonstrated in [47]. However, our typical LNOI device dimensions are an order of magnitude smaller than proton-exchange lithium niobate circuits, which could create challenges during fabrication. Another improvement would come from adding input and output single qubit gates for performing process and state tomography, violating the CHSH inequality and preparing arbitrary two-qubit states. In this work, we highlight the potential for photonic quantum gates to be implemented in continuously coupled waveguide arrays, offering a more compact solution compared to existing architectures and opening new pathways towards the development of more complex multi-photon circuits in a single interaction region.

Data availability statement

All data that support the findings of this study are included within the article (and any supplementary files).

Acknowledgment

We acknowledge support for characterization of our samples from the Scientific Center of Optical and Electron Microscopy ScopeM and from the cleanroom facilities BRNC and FIRST of ETH Zurich and IBM Ruschlikon. R J C acknowledges support from the Swiss National Science Foundation under the Ambizione Fellowship Program (Project Number 208707). R G acknowledges support from the European Space Agency (Project Number 4000137426), the Swiss National Science Foundation under the Bridge Program (Project Number 194 693), the European Research Council (Project Number 714837), and Horizon 2020 (ELENA Consortium, Project Number 101016138).

Conflict of interest

The authors declare no competing financial or non-financial interests.

Author contributions

R J C conceived the experiment. R J C and S H designed the waveguide array. G F and F K fabricated the lithium niobate-on-insulator waveguide samples. R J C performed the optical measurements, data analysis and wrote the original draft of the manuscript. R G supervised the project. All authors contributed to revising the manuscript.

ORCID iDs

Robert J Chapman https://orcid.org/0000-0002-0368-8483
Samuel Häusler https://orcid.org/0000-0002-3798-5259
Giovanni Finco https://orcid.org/0000-0002-1218-1924
Fabian Kaufmann https://orcid.org/0000-0002-3164-8833
Rachel Grange https://orcid.org/0000-0001-7469-9756

References

[1] O'Brien J L 2007 Optical quantum computing *Science* **318** 1567–70
[2] Slussarenko S and Pryde G J 2019 Photonic quantum information processing: a concise review *Appl. Phys. Rev.* **6** 041303
[3] Aspuru-Guzik A and Walther P 2012 Photonic quantum simulators *Nat. Phys.* **8** 285–91
[4] Gisin N and Thew R 2007 Quantum communication *Nat. Photon.* **1** 165–71
[5] Pirandola S, Bardhan B R, Gehring T, Weedbrook C and Lloyd S 2018 Advances in photonic quantum sensing *Nat. Photon.* **12** 724–33
[6] Ladd T D, Jelezko F, Laflamme R, Nakamura Y, Monroe C and O'Brien J L 2010 Quantum computers *Nature* **464** 45–53
[7] Knill E, Laflamme R and Milburn G J 2001 A scheme for efficient quantum computation with linear optics *Nature* **409** 46–52
[8] Ralph T C, Langford N K, Bell T B and White A G 2002 Linear optical controlled-NOT gate in the coincidence basis *Phys. Rev.* A **65** 062324
[9] O'Brien J L, Pryde G J, White A G, Ralph T C and Branning D 2003 Demonstration of an all-optical quantum controlled-NOT gate *Nature* **426** 264–7
[10] Politi A, Cryan M J, Rarity J G, Siyuan Y and O'Brien J L 2008 Silica-on-silicon waveguide quantum circuits *Science* **320** 646–9
[11] Reck M, Zeilinger A, Bernstein H J and Bertani P 1994 Experimental realization of any discrete unitary operator *Phys. Rev. Lett.* **73** 58–61
[12] Clements W R, Humphreys P C, Metcalf B J, Kolthammer W S and Walmsley I A 2016 Optimal design for universal multiport interferometers *Optica* **3** 1460–5

[13] Kraus Y E, Lahini Y, Ringel Z, Verbin M and Zilberberg O 2012 Topological states and adiabatic pumping in quasicrystals *Phys. Rev. Lett.* **109** 106402
[14] Hafezi M, Mittal S, Fan J, Migdall A and Taylor J M 2013 Imaging topological edge states in silicon photonics *Nat. Photon.* **7** 1001–5
[15] Rechtsman M C, Zeuner J M, Plotnik Y, Lumer Y, Podolsky D, Dreisow F, Nolte S, Segev M and Szameit A 2013 Photonic Floquet topological insulators *Nature* **496** 196–200
[16] Mittal S, Goldschmidt E A and Hafezi M 2018 A topological source of quantum light *Nature* **561** 502–6
[17] Zilberberg O, Huang S, Guglielmon J, Wang M, Chen K P, Kraus Y E and Rechtsman M C 2018 Photonic topological boundary pumping as a probe of 4D quantum Hall physics *Nature* **553** 59–62
[18] Tambasco J-L, Corrielli G, Chapman R J, Crespi A, Zilberberg O, Osellame R and Peruzzo A 2018 Quantum interference of topological states of light *Sci. Adv.* **4** eaat3187
[19] Schwartz T, Bartal G, Fishman S and Segev M 2007 Transport and Anderson localization in disordered two-dimensional photonic lattices *Nature* **446** 52–55
[20] Lahini Y, Avidan A, Pozzi F, Sorel M, Morandotti R, Christodoulides D N and Silberberg Y 2008 Anderson localization and nonlinearity in one-dimensional disordered photonic lattices *Phys. Rev. Lett.* **100** 013906
[21] Martin L *et al* 2011 Anderson localization in optical waveguide arrays with off-diagonal coupling disorder *Opt. Express* **19** 13636–46
[22] Crespi A, Osellame R, Ramponi R, Giovannetti V, Fazio R, Sansoni L, De Nicola F, Sciarrino F and Mataloni P 2013 Anderson localization of entangled photons in an integrated quantum walk *Nat. Photon.* **7** 322–8
[23] Blanco-Redondo A, Bell B, Oren D, Eggleton B J and Segev M 2018 Topological protection of biphoton states *Science* **362** 568–71
[24] Perez-Leija A, Keil R, Kay A, Moya-Cessa H, Nolte S, Kwek L-C, Rodríguez-Lara B M, Szameit A and Christodoulides D N 2013 Coherent quantum transport in photonic lattices *Phys. Rev.* A **87** 012309
[25] Chapman R J, Santandrea M, Huang Z, Corrielli G, Crespi A, Yung M-H, Osellame R and Peruzzo A 2016 Experimental perfect state transfer of an entangled photonic qubit *Nat. Commun.* **7** 11339
[26] Gräfe M, Heilmann R, Perez-Leija A, Keil R, Dreisow F, Heinrich M, Moya-Cessa H, Nolte S, Christodoulides D N and Szameit A 2014 On-chip generation of high-order single-photon W-states *Nat. Photon.* **8** 791–5
[27] Schreiber A, Cassemiro K N, Potoček V, Gábris A, Mosley P J, Andersson E, Jex I and Silberhorn C 2010 Photons walking the line: a quantum walk with adjustable coin operations *Phys. Rev. Lett.* **104** 050502
[28] Defienne H, Barbieri M, Walmsley I A, Smith B J and Gigan S 2016 Two-photon quantum walk in a multimode fiber *Sci. Adv.* **2** e1501054
[29] Peruzzo A *et al* 2010 Quantum walks of correlated photons *Science* **329** 1500–3
[30] Lahini Y, Steinbrecher G R, Bookatz A D and Englund D 2018 Quantum logic using correlated one-dimensional quantum walks *npj Quantum Inf.* **4** 1–7
[31] Zhu D *et al* 2021 Integrated photonics on thin-film lithium niobate *Adv. Opt. Photonics* **13** 242–352
[32] Wang C, Zhang M, Chen X, Bertrand M, Shams-Ansari A, Chandrasekhar S, Winzer P and Lončar M 2018 Integrated lithium niobate electro-optic modulators operating at CMOS-compatible voltages *Nature* **562** 101–04
[33] Juanjuan L, Surya J B, Liu X, Bruch A W, Gong Z, Yuntao X and Tang H X 2019 Periodically poled thin-film lithium niobate microring resonators with a second-harmonic generation efficiency of 250 000%/W *Optica* **6** 1455–60
[34] Guo Q, Sekine R, Ledezma L, Nehra R, Dean D J, Roy A, Gray R M, Jahani S and Marandi A 2022 Femtojoule femtosecond all-optical switching in lithium niobate nanophotonics *Nat. Photon.* **16** 625–31
[35] Zhao J, Chaoxuan M, Rüsing M and Mookherjea S 2020 High quality entangled photon pair generation in periodically poled thin-film lithium niobate waveguides *Phys. Rev. Lett.* **124** 163603
[36] Kaufmann F, Finco G, Maeder A and Grange R 2023 Redeposition-free inductively-coupled plasma etching of lithium niobate for integrated photonics *Nanophotonics* **12** 8
[37] Krasnokutska I, Chapman R J, Tambasco J-L J and Peruzzo A 2019 High coupling efficiency grating couplers on lithium niobate on insulator *Opt. Express* **27** 17681–5
[38] Kang S, Zhang R, Hao Z, Jia D, Gao F, Fang B, Zhang G and Jingjun X 2020 High-efficiency chirped grating couplers on lithium niobate on insulator *Opt. Lett.* **45** 6651–4
[39] Lomonte E, Lenzini F and Pernice W H P 2021 Efficient self-imaging grating couplers on a lithium-niobate-on-insulator platform at near-visible and telecom wavelengths *Opt. Express* **29** 20205–16
[40] Chen B, Ruan Z, Fan X, Wang Z, Liu J, Chijun Li, Chen K and Liu L 2022 Low-loss fiber grating coupler on thin film lithium niobate platform *APL Photonics* **7** 076103
[41] Lomonte E, Stappers M, Krämer L, Pernice W H P and Lenzini F 2023 Scalable and efficient grating couplers on low-index photonic platforms enabled by cryogenic deep silicon etching (arXiv:2305.00907 [physics])
[42] Zheng Y *et al* 2023 Electro-optically programmable photonic circuits enabled by wafer-scale integration on thin-film lithium niobate *Phys. Rev. Res.* **5** 033206
[43] Maeder A, Kaufmann F, Pohl D, Kellner J and Grange R 2022 High-bandwidth thermo-optic phase shifters for lithium niobate-on-insulator photonic integrated circuits *Opt. Lett.* **47** 4375–8
[44] Chen P-K, Briggs I, Cui C, Zhang L, Shah M and Fan L 2023 Adapted poling to break the nonlinear efficiency limit in nanophotonic lithium niobate waveguides (arXiv:2307.11671 [physics])
[45] Clauser J F, Horne M A, Shimony A and Holt R A 1969 Proposed experiment to test local hidden-variable theories *Phys. Rev. Lett.* **23** 880–4
[46] Hoch F *et al* 2021 Reconfigurable continuously-coupled 3D photonic circuit for Boson Sampling experiments *npj Quantum Inf.* **8** 55
[47] Youssry A, Yang Y, Chapman R J, Haylock B, Lenzini F, Lobino M and Peruzzo A 2023 Experimental graybox quantum system identification and control (arXiv:2206.12201 [physics, physics:quant-ph])